Optothermal response of a single silicon nanotip

A. Vella,[1,*] D. Shinde,[1] J. Houard,[1] E. Silaeva,[1] L. Arnoldi,[1] I. Blum,[1] L. Rigutti,[1] E. Pertreux,[2] P. Maioli,[2] A. Crut,[2] and N. Del Fatti[2]

[1]*Groupe de Physique des Matériaux UMR CNRS 6634, Normandie Université, Université-INSA de Rouen, Avenue de l'Université BP 12, 76801 Saint Etienne du Rouvray, France*

[2]*FemtoNanoOptics Group, Université de Lyon, Institut Lumière Matière UMR5306, Université Lyon 1-CNRS, 69622 Villeurbanne, France*

The optical properties and thermal dynamics of conical single silicon nanotips are experimentally and theoretically investigated. The spectral and spatial dependencies of their optical extinction are quantitatively measured by spatial modulation spectroscopy (SMS). A nonuniform optical extinction along the tip axis and an enhanced near-infrared absorption, as compared to bulk crystalline silicon, are evidenced. This information is a key input for computing the thermal response of single silicon nanotips under ultrafast laser illumination, which is investigated by laser assisted atom probe tomography (La-APT) used as a highly sensitive temperature probe. A combination of these two experimental techniques and comparison with modeling also permits us to elucidate the impact of thermal effects on the laser assisted field evaporation process. Extension of this coupled approach opens up future perspectives for the quantitative study of the optical and thermal properties of a wide class of individual nano-objects, in particular elongated ones such as nanotubes, nanowires, and nanocones, which constitute promising nanosources for electron and/or ion emission.

I. INTRODUCTION

Sharp pointed needles with nanometric dimensions (named nanotips) are nowadays present in many nanoscale systems such as plasmonic devices [1], gas sensors [2], supercapacitors [3], and structured surfaces for solar cells and photovoltaic applications [4]. Moreover, nanotips are used in many techniques of materials analysis and structuring such as scanning tunneling microscopy, atomic force microscopy, or near-field imaging techniques such as apertureless near-field optical microscopy [5–7] or scanning thermal microscopy [8]. The interaction between an ultrashort laser pulse and a nanometric tip is also used to create coherent and ultrafast electron sources [9,10] or to control field ionization of nonmetallic materials [11,12]. In all these applications, the laser-tip interaction not only induces linear and nonlinear optical effects (such as field enhancement, second harmonic generation, or surface optical rectification) [13,14], but also leads to a heating of the tip [15]. The evaluation of the absorption and thermal dynamics of this structure is therefore critical to estimate the contributions of thermal and optical effects. For example, heating of plasmonic devices induces a change of their refractive index and hence a degradation of their performances [1]. Similarly, thermally assisted ejection of electrons (or ions) affects the quality of ultrafast emission of electron (or ion) nanosources [16,17]. The contribution of the thermal effects also has to be precisely quantified to correctly describe nanoscale photoinduced processes ranging from photopolymerization to cancer photothermal therapy [18].

Up to now, the study of the thermal response of a nanotip to laser illumination was always based on numerical calculation of its optical response (i.e., absorption and scattering of the incident laser beam). To quantify the contribution of thermal effects to electron emission and ion evaporation, the computed absorption maps were then used as an initial condition for heat diffusion equations [16,17,19]. In this work, we directly measure the optical response of a single silicon nanotip by spatial modulation spectroscopy (SMS) [20,21]. This original technique has been previously used to detect individual zero-dimensional (0D) absorbing nano-objects and measure their absolute optical extinction spectra [22–28]. SMS has also been successfully exploited to investigate one-dimensional (1D) cylindrical nano-objects such as single metal nanowires and carbon nanotubes (with length much larger and diameter much smaller than the size of the focused light beam), providing access to their optical response [21,29,30]. In the present experiments, a nonuniform optical extinction along the nanotip axis is experimentally evidenced. By comparison with theoretical calculations, a strong modification of the optical properties of silicon nanotips in the near infrared (IR) with respect to those tabulated for bulk crystalline silicon is also pointed out.

These results provide key information for the investigation of the nanotip thermal dynamics, which is probed by laser assisted atom probe tomography (La-APT). In La-APT, the surface atoms of a nanotip, biased at about 10 kV, are field evaporated under the combined action of the strong static field generated at the apex of the sample (about 10 V/nm) and a femtosecond laser pulse. APT is a powerful tool for the analysis of materials, as it allows their three-dimensional (3D) imaging with near atomic resolution [12,31–36]. However, the fundamental process at the basis of La-APT of nonmetallic tips, i.e., laser-assisted field evaporation, remains unclear.

*angela.vella@univ-rouen.fr

Its surprising efficiency could be explained by two distinct scenarios associated with different time scales and physical mechanisms, i.e., thermal effects and static field-induced modification of nanotip properties. In the former scenario, laser energy absorption generates hot carriers all along the tip, whose relaxation and diffusion, as well as the diffusion of the generated heat, lead to a delayed heating of the tip apex, allowing evaporation to remain efficient on nanosecond time scales [37]. In the latter, the application of an intense static electric field leads to the accumulation of a high density of positive charges at the apex, which considerably enhances its optical absorption, inducing ultrafast heating followed by its cooling on a picosecond time scale [11].

A combination of these two experimental techniques on the same type of nano-objects permits us to elucidate the contribution of the induced thermal effects to the complex laser assisted field evaporation process. In particular, this work demonstrates that the nonuniform optical absorption along the conical nanotip and the subsequent heat diffusion are at the origin of the different measured kinetics of evaporation at nanosecond scale. These can be quantitatively reproduced using a complete model including the optical, thermal, and electronic properties of the nanotip, clarifying the dependence of the evaporation mechanism on illumination conditions and nanotip shape.

II. EXPERIMENTAL RESULTS AND DISCUSSION

Silicon nanotips were prepared by focused ion beam (FIB) annular milling from micrometer silicon posts (more details on the sample preparation procedure can be found in Ref. [38]). Their geometrical parameters (conical shape with apex radius R and semi-angle β) were deduced from electron microscopy observations.

A. Optical investigations on a single nanotip

The optical response of individual silicon nanotips was quantitatively investigated using SMS, a technique relying on the modulation of the position of a single nano-object inside the focal spot of a tightly focused light beam, which results in periodical variations of the transmitted (or reflected) light power [20,29]. A tunable Ti:sapphire oscillator combined with a visible optical parametric oscillator was used as the light source, allowing nanotip optical properties to be investigated in a broad spectral range (500–1000 nm wavelengths). Spatial modulation was performed orthogonally to the tip axis at $f = 1.5$ kHz frequency and lock-in detection was performed at $2f$. SMS optical transmission images with light polarization parallel to the nanotip axis were acquired by scanning the sample relatively to the light beam focused down to diffraction limit (about 0.7λ full-width at half-maximum) by a $100\times$ microscope objective.

SMS optical cartographies of a single conical silicon nanotip ($R = 40$ nm apex radius and $\beta = 3°$ semi-angle) are shown in Fig. 1(a) at three different illuminating wavelengths. The nanotip shows up as a main central line with two satellites of smaller amplitude, as previously observed for nanotubes [21,25,29]. However, conversely to such elongated nano-objects with uniform diameter, the amplitude of SMS signals

varies here in a nonmonotonic way along the nanotip axis [Figs. 1(a) and 1(b)]. It presents in particular a succession of three clear local maxima at $\lambda = 550$ nm, separated by 1600 nm distance. Similar behavior is measured at $\lambda = 750$ nm, where two main peaks appear with a separation of 2500 nm, while a single peak is observed at $\lambda = 950$ nm.

These spatial variations demonstrate inhomogeneous absorption and scattering of light along the tip of variable thickness, associated with local variations of the electromagnetic field inside the tip and to interference effects. To precisely understand their origin, we developed two types of calculations: (i) an analytical estimation of optical cross sections along the nanotip, using an approximate model based on Mie theory for cylinders under plane wave illumination [Fig. 1(c)] and (ii) specific numerical simulation of the SMS signals, using a complete finite-element model including the features of the experiment, i.e., focused illumination and modulation process [Fig. 1(d)]. In both calculations, nanotips were described by identical geometrical parameters and optical properties, considering a homogeneous air environment and the tabulated complex refractive index $\tilde{n} = (n + ik)$ of bulk crystalline silicon [39–41].

Analytical modeling was performed following the simplified approach described in Ref. [44] valid for cones of small semi-angle β. In this approximation, a thin transverse section of a conical tip (with apex radius R) at distance z from the apex is assumed to have the same optical response per unit length as that of an infinite cylinder [with diameter $D(z) = 2(R + z \tan \beta)$ increasing along the cone axis]. Its absorption, scattering, and extinction cross sections are thus accessible using Mie theory [45]. In the framework of this model, the scattering contribution is predicted to dominate over the absorption one (Fig. 2). Their sum, i.e., the extinction cross-section profiles computed for a silicon nanotip in air at the three wavelengths, are shown in Fig. 1(c) (black line). They display complex variations along the nanotip axis, related to the longitudinal variations of the tip diameter. They are characterized by multiple resonant sharp peaks (ripple structure) overlapping regular oscillations of a longer period (interference structure) [45].

The ripple structure is associated with a resonant behavior of specific electromagnetic modes (enhancement of an electromagnetic field for a specific diameter over wavelength ratios) and affects both absorption and scattering cross sections (Fig. 2). For the wavelengths considered here, the spatial extension of these hot spots is much smaller than the diffraction-limited size of a focused light beam. This hinders their detection by a far-field optical technique such as SMS (it may however be possible with higher-resolution near-field techniques). The disappearance of the ripple structure induced by optical resolution limitations is illustrated in Fig. 1(c) (red line), obtained by spatially convoluting the expected extinction cross section with the Gaussian intensity profile of the incident light beam.

The longer periodic structure in extinction is caused by a scattering effect [Figs. 2(b) and 2(c)]. It is usually interpreted as the result of far-field interferences between waves transmitted and diffracted by the scattering structure [45,46]. This simplified model developed for an infinite cylinder of diameter D and refractive index $n + ik$ leads to periodical
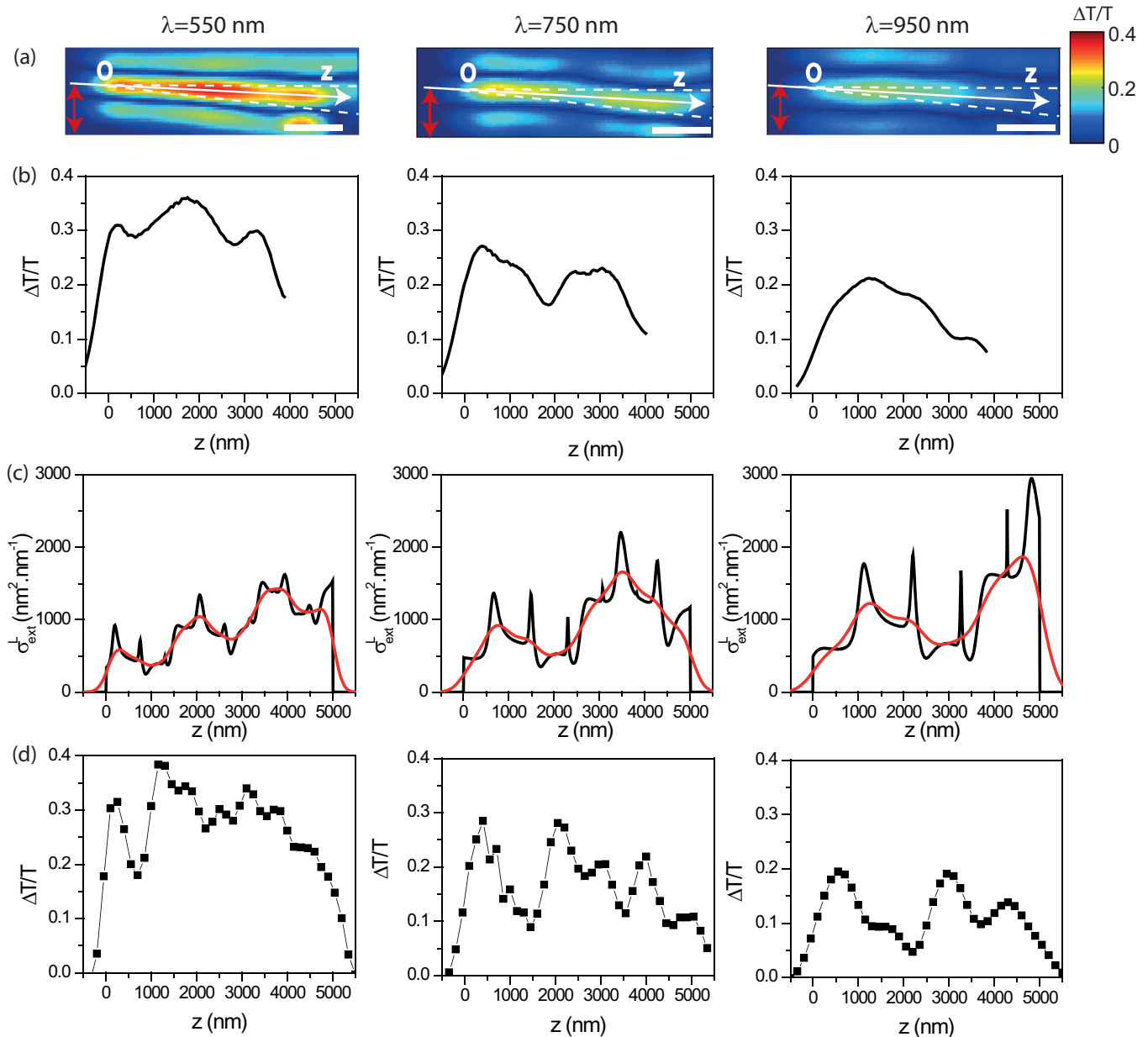
FIG. 1. SMS microscopy of a single silicon nanotip ($R = 40$ nm apex radius, $\beta = 3°$ semi-angle) illuminated at $\lambda = 550$ nm (left column), 750 nm (middle column), and 950 nm (right column). (a) Experimental SMS transmission images obtained with incident light polarized along the tip axis. The direction of modulation is indicated by red arrows and the actual nanotip position is shown by the white dashed lines. Scale bar: 1 μm. (b) SMS signal ($2f$ component $\Delta T/T$ of the modulated optical transmission change) profile along the tip axis [Oz axis in (a)]. (c) Extinction cross section per unit length profile $\sigma_{\text{abs}}^{L}(z)$ computed for a $L = 5$ μm nanotip following Mie theory for infinitely long cylinders and plane wave illumination (see main text). Black line: bare calculations, red line: convolution with a Gaussian intensity profile. (d) Complete finite-element modeling of experimental (b) SMS transmission profiles. All modeling uses the crystalline silicon refractive index [39–41].

variations of extinction efficiency (defined as the ratio of the extinction cross section per unit length and the nano-object diameter) with a period $\Delta D = \lambda/(n − 1)$. In a conical nanotip, taking into account the relation between the position z along the nanocone axis and the local diameter D, this periodicity translates into a spatial periodicity of $\Delta z = \lambda/[2(n − 1)\tan\beta]$, highlighting in particular the effect of the illuminating wavelength, in agreement with Mie theory. For the silicon nanocones considered here, this leads to Δz values of 1700, 2600, and 3500 nm for 550, 750, and 950 nm wavelengths, respectively,

thus involving spatial periodicities larger than the wavelength. Contrary to ripple oscillations, they can therefore be detected by diffraction-limited optical techniques, as demonstrated in Fig. 1(c) showing their persistence after convolution of Mie calculations with a Gaussian profile, in good qualitative agreement with experimental results. Note that the existence of strong oscillations in the extinction cross section also provides information on tip absorption, this effect being attenuated in the presence of a strongly absorbing material. This is illustrated by comparing the nanotip extinction profiles computed
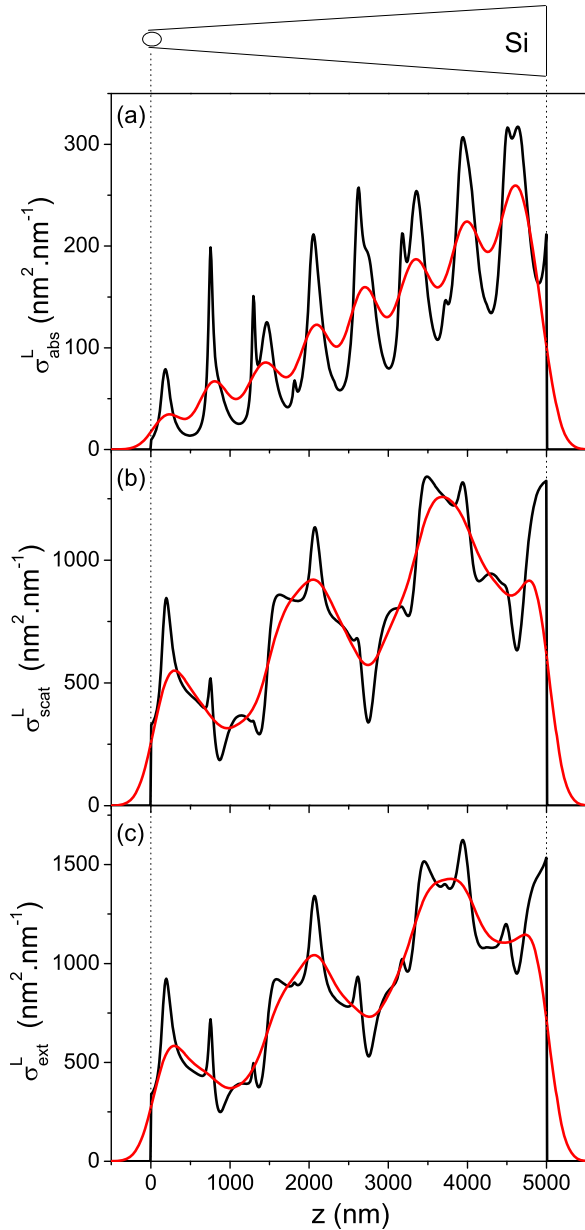
FIG. 2. Mie theory calculations for a $L = 5$ μm long silicon nanotip with $\beta = 3°$ semi-angle and $R = 40$ nm apex radius illuminated by a $\lambda = 550$ nm plane wave. Spatial profiles of (a) absorption, (b) scattering, and (c) extinction cross sections per unit length computed using Mie theory in the infinitely long cylinder approximation. Black lines: bare calculations, red lines: convolution with a Gaussian intensity profile of 0.7λ full-width at half-maximum.

using complex refractive index of crystalline [Fig. 1(c)] and amorphous silicon [Fig. 3(b)]. In the latter, the spatial features in a computed extinction cross section vanish at $\lambda = 550$ nm, where the amorphous silicon $k = 0.8$ is more than 20 times larger than the crystalline value (n values being close) [42,43]. This is in strong disagreement with experimental observations at the same wavelength, confirming that the optical response of nanotips in the visible can be well modeled using a crystalline silicon refractive index.

To go further into comparison between optical experiments and theory, a more quantitative model is necessary. As described above, the simple model explains the main spectral features, i.e., the regular succession of local maxima measured along the nanotip axis and the increase of their spacing with wavelength, but presents several limitations for a quantitative analysis of SMS signals in the presence of a nano-object with a size comparable to or larger than the spot size. It provides optical cross sections whose link with bare SMS signals (transmission changes) can be established for small (nanoparticles) or simple (nanowires) nano-object shapes, but is not obvious in the present case with large nanocones. In particular, this model which does not take into account the spatial modulation process at the basis of SMS, predicts a variation (overall increase of extinction far away from the apex) opposite to the experimental one (experimental decrease of SMS signal). Diffraction at the apex is also not considered and focused illumination is only crudely taken into account by *a posteriori* Gaussian convolution of results assuming plane wave illumination.

For a more detailed analysis of experiments, to overcome these issues, we developed a complete numerical model of SMS experiments using finite-element analysis. The approach that we used for modeling the optical response of nanotips presents large similarities with those used in our earlier finite-element studies on 3D-confined nano-objects [25,28]: simulations are performed in the scattered field formulation (i.e., defining the incident electromagnetic field and computing the scattered one induced by the investigated nanostructure), and the simulation domain is surrounded by perfectly matched layers to avoid spurious reflections at its border. However, the application of finite-element electromagnetic modeling to a system with one dimension much larger than the wavelength raises additional difficulties as compared to previous simulations on 3D-confined nano-objects. Indeed, the need of a spatial mesh much finer than the wavelength (about ten times in our simulations; we checked that results are independent of mesh size below this limit) induces high memory and computational time requirements and limits the length of the nanostructures that can be investigated. To minimize this limitation, cylindrical simulation domains were considered instead of the more commonly used spherical ones, after verification that this modification does not affect the computed electromagnetic fields. This enabled the modeling of nanostructures up to $\sim$5 μm length. Since the simulations described here are not standard, they were first benchmarked, in particular by comparing their results to those provided by Mie theory for infinite cylinders, in the case of plane wave illumination [Figs. 4(a) and 4(b)]. Absorption cross section per unit length was considered for this comparison as it is locally defined, allowing its full spatial profile to be numerically computed and compared with Mie predictions. The numerically computed average absorption of a long (5 μm) cylindrical nanowire was found to match that predicted by Mie theory for an infinite one [Fig. 4(a), note however that the finite cylinder length considered in numerical simulations induces a cavity effect which is not predicted for infinite systems, namely longitudinal oscillations of absorption along the cylinder axis, with an amplitude small near the nanowire center but much larger close to its ends]. Such agreement was obtained in
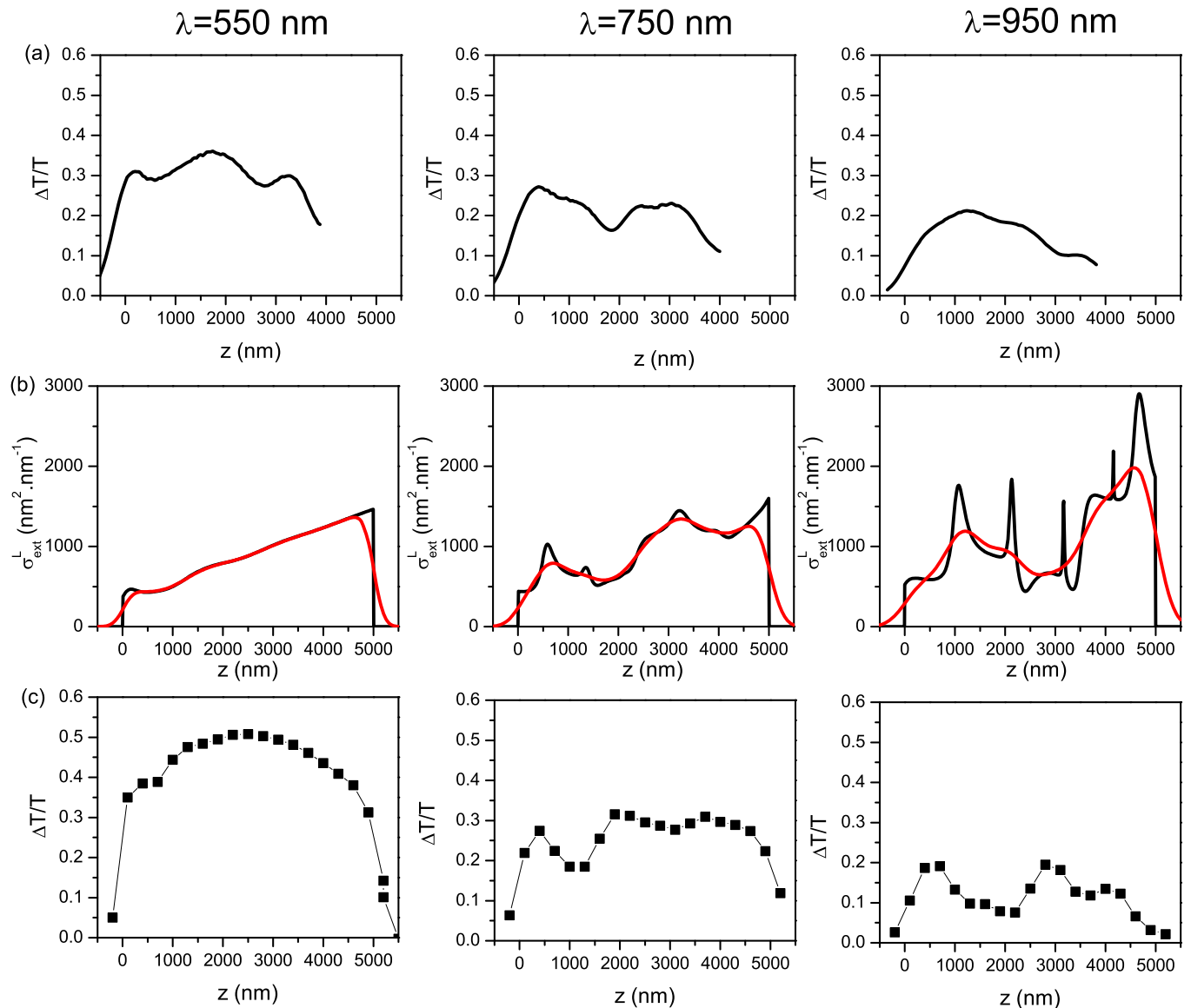
FIG. 3. Same as Fig. 1 but with modeling based on an amorphous silicon refractive index [42,43]. (a) Experimental SMS transmission profiles obtained at $\lambda = 550$ nm (left column), 750 nm (middle column), and 950 nm (right column) [same as Fig. 1(b)]. (b) and (c) Theoretical calculations for a $L = 5$ μm long silicon nanotip with $\beta = 3°$ semi-angle and $R = 40$ nm apex radius. (b) Extinction cross section per unit length profile computed using Mie theory for infinitely long cylinders and plane wave illumination. Black line: bare calculations, red line: convolution with a Gaussian intensity profile. (c) Complete finite-element modeling of experimental SMS transmission profiles.

the whole 0–400 nm nanowire diameter range, finite-element calculations thus yielding oscillations of the nanowire linear absorption cross section similar to those predicted by Mie theory [Fig. 4(b)]. Similar good agreement was also observed for nanotips [Fig. 4(c)]. In this case, the absorption profile computed by finite-element analysis shows a global rise overlapped to oscillations, which are well reproduced by Mie theory assuming that a thin slice of the nanotip has the same response per unit length as if it belonged to an infinite cylinder (thus demonstrating the validity of this assumption, proposed in Ref. [44] and used in the simplified optical analysis described above and in the thermal investigations constituting the second part of the paper), except at the large-diameter end of the tip. Analysis of SMS experiments was then carried out by considering a nanotip illuminated by a focused Gaussian beam.

Gaussian beams were defined with fifth-order corrections [47] to minimize spurious effects associated with the fact that they are not exact solutions of Maxwell equations. Finite-element computations were performed for different beam positions perpendicularly to the nanotip axis (in order to numerically mimic the spatial modulation process used in SMS) and along it [in order to model the experimental profiles shown in Fig. 1(b); the evolution of the absorbed fraction of the incident power as a function of Gaussian beam position along nanotip axis is shown in Fig. 4(d) and presents oscillations induced by diameter variations qualitatively similar to those of Figs. 4(b) and 4(c)]. For each beam position, the transmitted power was numerically deduced from the computed total electromagnetic field by integration of its Poynting vector in the forward direction, allowing estimation of the attenuation by comparison
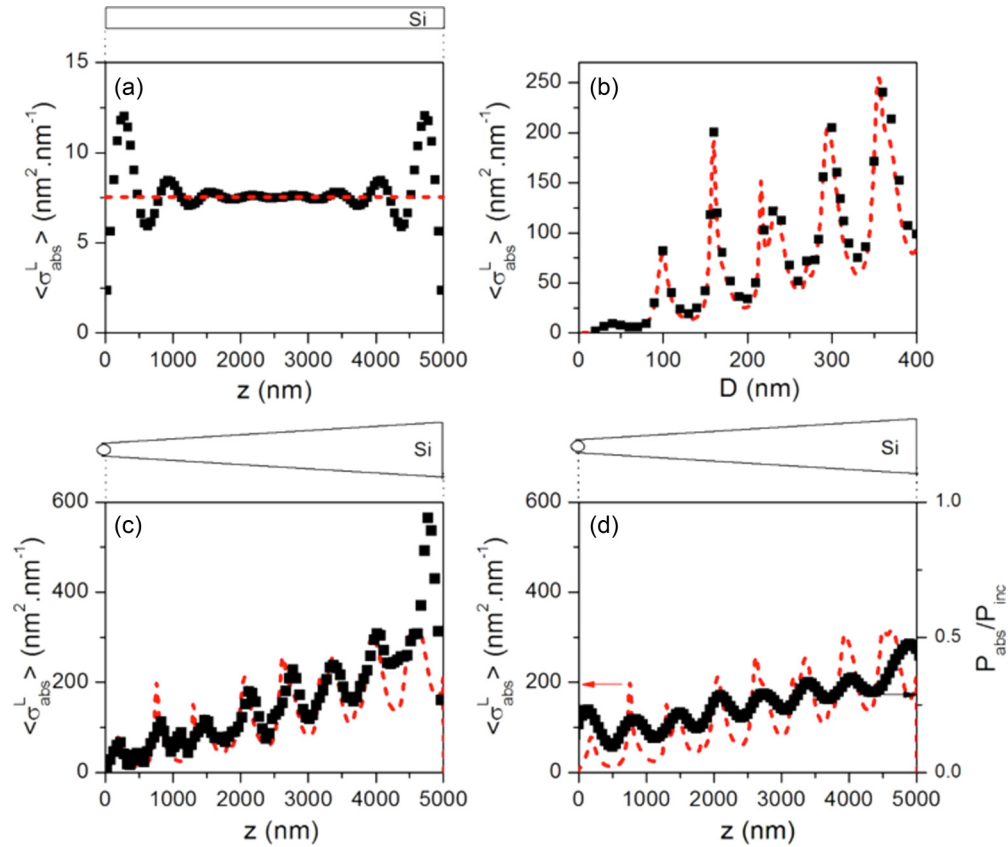
FIG. 4. Comparison of finite-element (black dots) and Mie (dashed red lines) calculations of the absorption cross section per unit length of elongated nano-objects illuminated by 550 nm wavelength light polarized along their large axis. (a) and (b) 5 μm long cylindrical Si nanowire illuminated by a plane wave. (a) Finite-element computed absorption profile for 50 nm nanowire diameter (each dot corresponds to an average over a 50 nm thickness) and linear absorption cross-section value predicted by Mie theory for an infinite cylinder of same diameter. (b) Dependence on nanowire diameter of the computed average linear absorption cross sections. (c) and (d) Si nanotip (same geometrical parameters as in Fig. 2). (c) Absorption profiles computed for plane wave illumination using finite-element analysis (each dot corresponds to an average over a 50 nm thickness) and Mie theory in the infinitely long cylinder approximation. (d) Absorbed power fraction (defined as the ratio between the absorbed power P_{abs} and the total one carried by the incident Gaussian beam P_{inc}) profile computed for Gaussian beam illumination using finite-element analysis (each dot corresponds to a distinct Gaussian beam position along the nanotip axis). The Mie-computed profile of absorption cross section per unit length is the same as in (c).

with the total power carried by the incident Gaussian beam. To interpret experiments, SMS signals along the nanotip axis were then simulated by computing the $2f$ Fourier component of transmitted power for a sinusoidal variation of Gaussian beam position in the transverse direction. Only nanotips shorter than the experimentally investigated ones could be considered in the modeling. Such tip truncation is expected to preclude reliable comparison between experimental and simulated signals far away from the tip apex. However, we found that signals simulated near the tip apex (typically for distances z below half of the considered tip length) are independent of the considered tip length and can thus be reliably compared with experiments.

The simulated SMS profile at $\lambda = 550$ nm using a crystalline silicon refractive index is shown in Fig. 1(d). It is in good quantitative agreement with the experimental one [Fig. 1(b)], the amplitude of the SMS signal (relative transmission change $\Delta T/T \simeq 0.3$) being in particular excellently reproduced. An oscillatory profile is also predicted, with local maxima at positions close to those experimentally observed [similarly to the simple model calculations, this agreement disappears when

using an amorphous silicon refractive index with a strongly absorptive imaginary part, see Fig. 3(c)]. While the agreement remains still quite good at $\lambda = 750$ nm, a discrepancy is present between measured and simulated SMS signals at $\lambda = 950$ nm, where the latter predicts a marked oscillatory behavior not detected in experiments (Fig. 1). At this wavelength, a better agreement is obtained in the region close to the apex ($z < 2$ μm) if the imaginary part of the nanotip refractive index used in the simulations is increased from the $k = 10^{-3}$ value for pure silicon to $k \simeq 0.5$, resulting in smoother computed oscillations (see Fig. 5). It suggests that the optical properties of the investigated nanotips are correctly described using the tabulated refractive index of bulk crystalline silicon only in the low wavelength range, and should be corrected in the infrared (note that numerical results for the region $z > 2$ μm are affected by tip truncation, however, this region does not influence the apex thermal kinetics investigated below on a few nanoseconds time scale).

This modification is confirmed by the huge increase of the optical absorption coefficient in the IR spectral domain that was
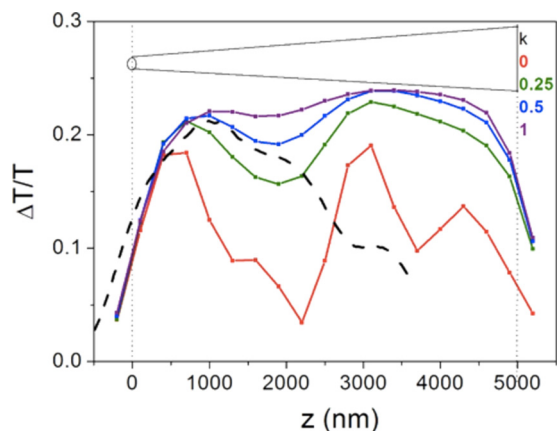
FIG. 5. Dependence of the computed SMS transmission profiles on the imaginary part of the tip refractive index (k) at $\lambda = 950$ nm wavelength. The calculations performed for the silicon tip shown in Fig. 1(d) (using bulk crystalline silicon $n = 3.59$ and $k = 10^{-3}$ [40,41]), are here computed for increasing values of k: $k = 0$ (red symbols and line), 0.25 (green), 0.5 (blue), and 1 (purple). Experimental measurement at $\lambda = 950$ nm is shown as a dashed black line.
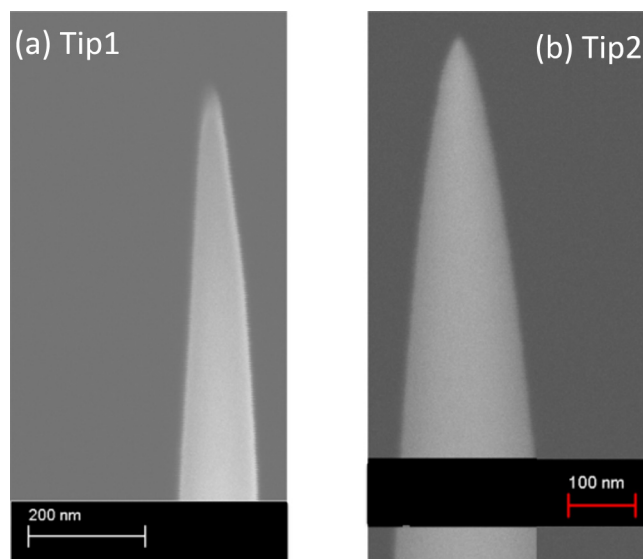

FIG. 6. (a) and (b) Scanning electron microscopy (SEM) of the two silicon nanotips investigated by La-APT, with same $R = 25$ nm apex radius, $\beta_1 = 3.5°$ (tip 1) and $\beta_2 = 6.8°$ (tip 2) semi-angles.

already reported on silicon fibers prepared by FIB [48,49]. This change in the optical properties of the nanotip is attributed to the FIB annular milling process. During this process, Ga ions are projected on the samples with an energy ranging from 5 to 30 keV and they produce an amorphous layer at the samples surface with a thickness that depends on the ions energy and the fluence [50,51]. Ga ions are also implanted inside the silicon sample and constitute crystallographic defects which contribute to the change of the optical properties of the samples by several physical effects such as free-carrier absorption [52]. In such a case, the change of the optical absorption increases with the laser wavelength and is thus stronger in the IR domain [53]. Moreover, the presence of defects can increase absorption due to transition between one band and the corresponding impurity level [52], which is higher in IR domain, as reported for Ga ions implantation by Hell *et al.* [54].

These optical measurements provide crucial information for La-APT experiments, which are very sensitive to the thermal dynamics of nanotips and thus to their initial absorption profile.

B. Thermal investigations

The thermal kinetics of these nanotips after an ultrafast laser illumination were investigated by La-APT. The APT instrument used in this study is a linear atom probe with a flight length of ~ 10 cm in which single ions emitted from the nanotip hit a position sensitive detector. Experiments are performed at 80 K under ultrahigh vacuum conditions ($<10^{-7}$ Pa). The laser system is a femtosecond oscillator with a regenerative amplifier ($\lambda = 1030$ nm) operating at 100 kHz and generating pulses of 500 fs with a tunable energy of up to 10 μJ/pulse. Using SHG (second harmonic generation), the laser wavelength can be converted to 515 nm. The optical setup and more details can be found in Ref. [55]. The linear polarized laser beam is slightly focused on the silicon tip with a spot diameter of 100 μm at 1030 nm and 50 μm at 515 nm. The impact position on the

detector and the time of flight are recorded for each detected ion.

Two silicon tips were analyzed. The two tips have similar apex radius $R = (25 \pm 2)$ nm but different cone semi-angle of $\beta_1 = (3.5 \pm 0.5)°$ for tip 1, and $\beta_2 = (6.8 \pm 0.5)°$ for tip 2 [electron microscopy images are shown Figs. 6(a) and 6(b)]. Total mass spectra for these two investigated nanotips, showing evaporation of silicon ions, are shown in Fig. 7.

The time-of-flight spectra of the main peak, which corresponds to Si^{2+} ions, are shown in Fig. 8 (the origin $t = 0$ corresponds to the arrival time of the laser pulse). For tip 1 illuminated at $\lambda = 515$ nm [Fig. 8(b)], a first narrow peak is followed by a delayed and broad signal, with a maximum about
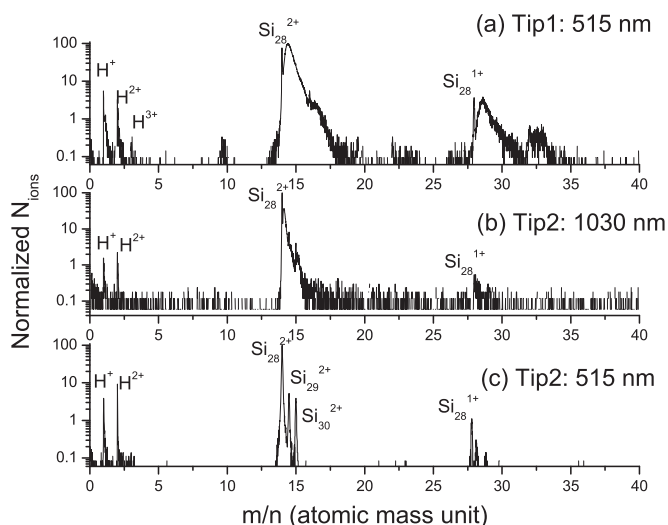

FIG. 7. Normalized number of detected ions N_{ions} per pulse as a function of their mass to charge m/n ratio (a) for $\lambda = 515$ nm laser pulses on tip 1, (b) for $\lambda = 1030$ nm pulses on tip 2, and (c) for $\lambda = 515$ nm pulses on tip 2. Laser fluences are reported in Table I.
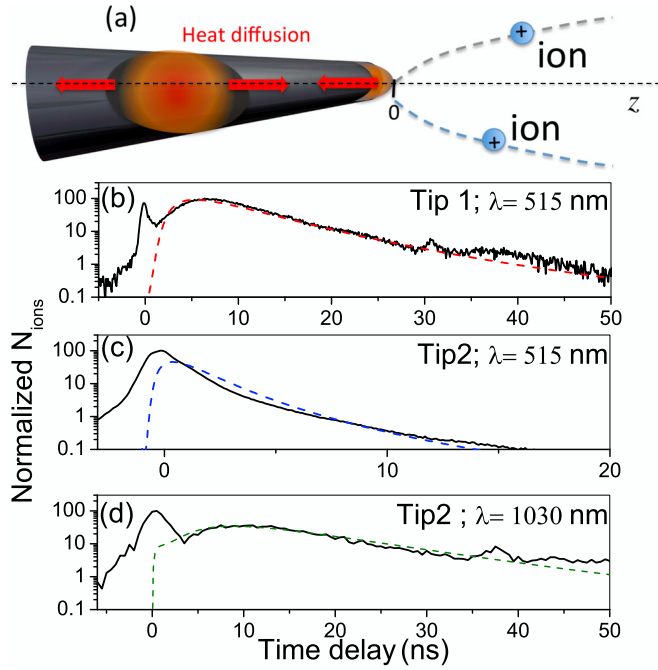
FIG. 8. (a) Schematic representation of the nonuniform heating of the silicon nanotip induced by laser absorption and the subsequent slow ion evaporation process. (b)–(d) Normalized number of evaporated ions per pulse as a function of time after interaction with the laser pulse, experimentally measured (solid black lines) and theoretically calculated (dashed red, blue, and green lines). Laser fluences are reported in Table I.

5 ns after laser excitation. However, a single peak followed by a nanosecond decay is measured for tip 2 at the same wavelength [Fig. 8(c)]. When changing the wavelength to λ = 1030 nm for tip 2, a kinetics similar to tip 1, but with a slower rise time (maximum at about 9 ns), is recovered [Fig. 8(d)]. The short time scale narrow peak is associated with the fast field evaporation process of surface atoms [56,57] and will not be discussed here. The slow thermal evaporation can induce a delayed rise time signal, because it requires heat diffusion to the apex (where atoms are field evaporated) from the regions which are the most efficiently heated by laser absorption, as schematically represented in Fig. 8(a). In this situation, the number of evaporated ions per pulse follows an Arrhenius law [58]:

$$N_{\text{ions}}(t) = \kappa \exp\left(-\frac{Q}{k_B T_s(t)}\right), \qquad (1)$$

where κ depends on different parameters including the number of atoms located at kink sites at the tip surface (which have the highest probability of evaporation), applied dc field, and detector efficiency; Q is the field-dependent activation energy and $T_s(t)$ is the surface tip temperature at the apex. The amplitude and position of the maximum of the broad signal thus provide information on the temperature of the tip apex and its temporal evolution, which are investigated here.

To model the evolution of the silicon nanotip temperature after illumination by the laser pulse, knowledge of nanotip linear absorption is crucial. Upon laser energy absorption, electrons are promoted to the silicon conduction band. Their subsequent

TABLE I. Model parameters

Quantity	Symbol	Value
Ambipolar diffusion coefficient	D_{e-h}	18 cm^2/s
Auger recombination coefficient	C_A	10^{-31} cm^6/s
Lattice thermal conductivity	K_l	see Ref. [60]
Lattice specific heat capacity	C_l	see Ref. [62]
Band gap	E_{gap}	1.1 eV
Refractive index: 515 nm	$\tilde{n}$	$4.19 + 0.036i$
1030 nm		$3.56 + 0.00024i$
1030 nm	$\tilde{n}_{\text{mod}}$	$3.56 + 0.5i$
Incident fluence: 515 nm	F_0	2.5 mJ/cm^2 (tip 1)
515 nm		1.75 mJ/cm^2 (tip 2)
1030 nm		5 mJ/cm^2 (tip 2)

relaxation due to carrier-phonon coupling and Auger recombination of the generated electron-hole pairs lead to the heating of the silicon lattice. Due to the inhomogeneous distribution of the absorbed energy along the nanotip (as previously demonstrated by the optical experiments), diffusion of carriers and heat contributes to the evolution of the temperature at the tip apex. Description of these processes requires resolution of a system of coupled equations for spatially and temporally dependent density of electron-hole pairs n_{e-h} and lattice temperature T_l [59]. The solution of the given problem in three dimensions is very expensive computationally. Thus, one-dimensional equations taking into account the variation of the tip geometrical cross-section $S(z)$ along z direction are considered:

$$\frac{\partial n_{e-h}}{\partial t} = \frac{1}{S(z)} \frac{\partial}{\partial z}\left(S(z) D_{e-h} \frac{\partial n_{e-h}}{\partial z}\right) - R_A,$$

$$C_l \frac{\partial T_l}{\partial t} = \frac{1}{S(z)} \frac{\partial}{\partial z}\left(S(z) K_l \frac{\partial T_l}{\partial z}\right) + E_{\text{gap}} R_A, \qquad (2)$$

where $R_A = C_A n_{e-h}^3$ corresponds to the rate of carrier losses due to Auger recombination, D_{e-h} is the ambipolar carrier diffusion coefficient, C_l is the lattice temperature-dependent specific heat capacity, K_l is the temperature-dependent conductivity taking into account nanowirelike shape and the presence of an amorphous layer at the surface of the tip [60], and E_{gap} is the band gap energy (see Table I for parameters of the model and experimental conditions). Boundary conditions include zero carrier diffusion current at the apex and at the base of the tip ($\frac{\partial n_{e-h}}{\partial z} = 0$), i.e., carriers do not leave the tip through its boundaries. The heat diffusion current is also zero at the apex ($\frac{\partial T_l}{\partial z} = 0$) since there is no heat exchange between the tip and the surrounding vacuum. The temperature at the base is kept constant at 80 K.

The initial carrier density n_{e-h}^0, photoexcited by interband absorption of the laser pulse, writes as

$$n_{e-h}^0(z) = \frac{\langle u_{\text{abs}}(z)\rangle}{\hbar\omega} = \frac{F_0 \sigma_{\text{abs}}^L(z)}{\hbar\omega S(z)}, \qquad (3)$$

where $\hbar\omega$ is the photon energy at the illuminating wavelength and $\langle u_{\text{abs}}(z)\rangle$ is the absorbed energy density per pulse computed from the incident fluence F_0 and the tip absorption cross-section per unit length [Figs. 9(a) and 9(b)]. As suggested by SMS analysis, a modified refractive index $\tilde{n}_{\text{mod}} = 3.56 + 0.5i$ was also considered in the calculations of $\sigma_{\text{abs}}^L(z)$ at
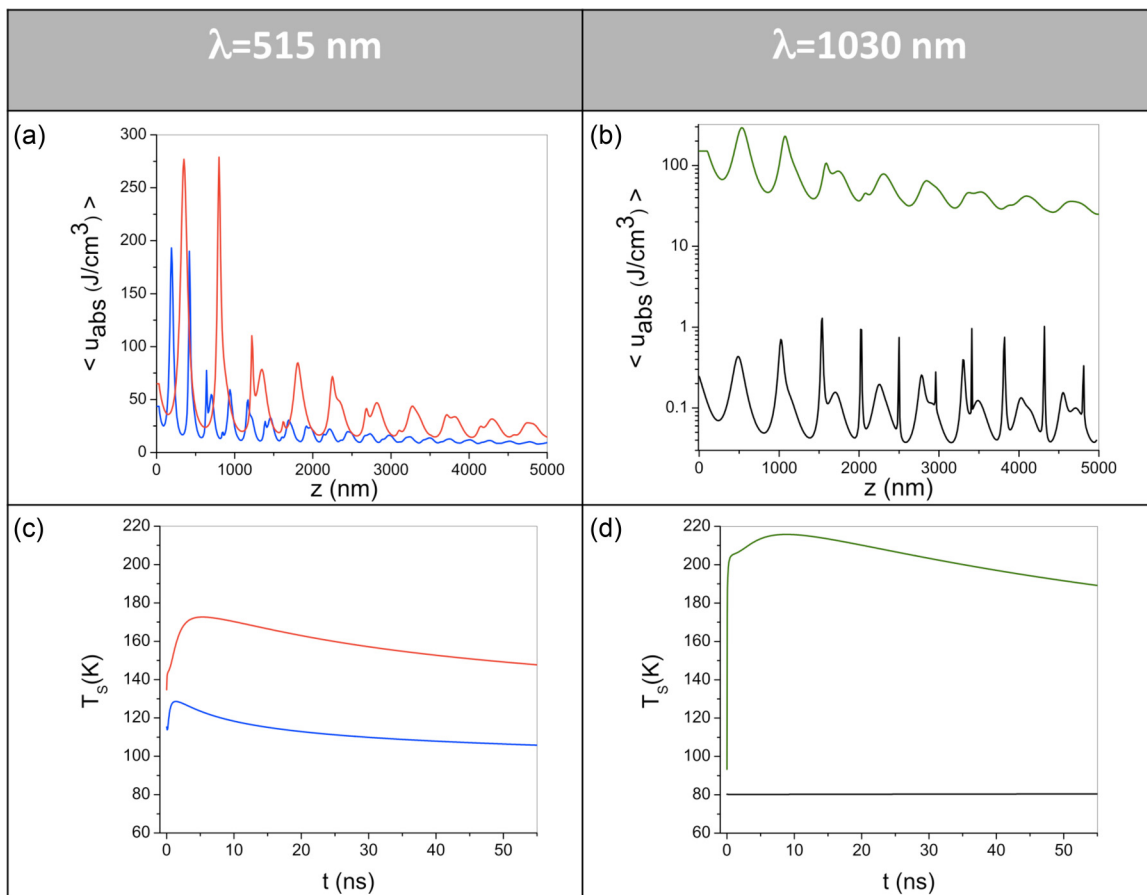
FIG. 9. (a) Absorbed energy densities (averaged over tip cross section) following the illumination at $\lambda = 515$ nm of tip 1 (red line) and tip 2 (blue line), computed using Mie theory for cylinders with the $\tilde{n} = 4.19 + 0.036i$ refractive index of pure silicon. (b) Computed absorbed energy density at $\lambda = 1030$ nm along tip 2, using $\tilde{n} = 3.56 + 0.00024i$ (black line) and modified $\tilde{n}_{\mathrm{mod}} = 3.56 + 0.5i$ (green line) [40,41]. The experimental values of laser fluence indicated in Table I were used in these simulations. (c) and (d) Resulting temporal evolutions of the temperature at the tip surface after illumination $T_s(t)$, computed using the model described in the main text [same color code as in (a) and (b)].

$\lambda = 1030$ nm, to take into account modifications induced by FIB [Fig. 9(b)].

At the first stage of lattice heating, the laser-generated carriers transfer their excess energy ($\hbar\omega - E_{\mathrm{gap}}$) to the phonon system within a few picoseconds [61]. During this time, carrier diffusion is negligible and the lattice is rapidly heated from 80 K, the tip base temperature, to $T_0(z)$, the initial condition for lattice temperature in Eq. (2):

$$\int_{80\,\mathrm{K}}^{T_0(z)} C_l(T)\,dT = n_{e-h}^0(z)(\hbar\omega - E_{\mathrm{gap}}). \tag{4}$$

Note that carrier drift in the applied dc field is here neglected. This field being screened inside semiconductor and dielectric tips within a few picoseconds after laser illumination [53], does not contribute to the delayed evaporation taking place a few nanoseconds after the laser pulse, during which electrons and holes move in pair by ambipolar diffusion with coefficient D_{e-h}.

Equations (2) are then numerically solved using these initial conditions for carriers and lattice temperature, for the two silicon nanotips illuminated in the visible and IR. Figure 9 shows the simulated temperature evolution at the apex of the silicon nanotips $T_l(z = 0) = T_s$ after interaction with the laser

pulse at $\lambda = 515$ nm for tip 1 and tip 2, and $\lambda = 1030$ nm for tip 2. From the computed $T_s(t)$, we fit the experimental time-of-flight spectra of Figs. 8(b)–8(d) using Eq. (1) and by adjusting the value of the activation energy Q for each nanotip.

At $\lambda = 515$ nm on tip 1 and tip 2, a good agreement between experimental and theoretical results is obtained for $Q_1 = (0.55 \pm 0.01)$ eV and $Q_2 = (0.50 \pm 0.02)$ eV, respectively. The different values of Q obtained for the two tips are due to the different conditions in La-APT. In fact the charge state ratio (CSR), defined as the ratio of detected ions Si^{1+} to Si^{2+}, increases from 1% to 4% from tip 2 to tip 1 at $\lambda = 515$ nm (Fig. 7). This variation of the CSR is associated with the variation of the surface field as calculated by Kingham [63]. Hence, an increase from 1% to 4% of CSR corresponds to a decrease of the field (and an increase of the barrier Q) for tip 1 as compared to tip 2 of 10%. This is consistent with our fits of experimental time-of-flight signals ($Q_1 = 1.1Q_2$). Note that, in the visible, this good agreement between experimental and theoretical results is obtained in both La-APT and SMS experiments by considering the crystalline bulk optical index for theoretical calculations.

However, at $\lambda = 1030$ nm, considering the refractive index of bulk crystalline silicon $\tilde{n} = 3.56 + 0.00024i$ [40,41], a

maximum surface temperature $T_s^{\max} = 80.1$ K is expected to be reached at time delay $t = 60$ ns. This maximum temperature is too low to induce ion emission in La-APT and the delay is too long to match the delayed evaporation in Fig. 8(d). Conversely, considering the modified index $\tilde{n}_{\mathrm{mod}} = 3.56 + 0.5i$, as suggested by SMS analysis in infrared domain, the maximum temperature at the surface of tip 2 is $T_s^{\max} = 216$ K, reached at a delay time of about $t = 9$ ns after the arrival of the laser pulse [Fig. 9(d)]. Using this temperature evolution in Eq. (1), a good agreement between experimental and theoretical results can be reached, as shown in Fig. 8(d), for $Q_2 = (0.50 \pm 0.02)$ eV. This value of energy barrier is equal to the value obtained on the same tip at $\lambda = 515$ nm, in very good agreement with an almost constant CSR from 1030 to 515 nm on tip 2, as shown in the mass spectra. Note that for this Q_2 value, reproduction of the kinetics can still be obtained in the 0.3–1.5 range of k, highlighting the interest of SMS optical experiments for yielding more precise information on this parameter.

These experiments performed on different nanotip geometries and at different wavelengths demonstrate that the ionization kinetics measured by La-APT can be very well correlated with the optical absorption of these conical nanostructures, and their induced out-of-equilibrium thermal responses at the nanotip apex. In particular, for a fixed $\lambda = 515$ nm, the positions of the absorbed energy density maxima along the z axis are shifted when increasing the tip cone semi-angle from $3.5°$ (tip 1) to $6.8°$ (tip 2) [Fig. 9(a)]: the maxima are closer to the tip apex for a larger cone angle, inducing a faster increase of the apex surface temperature in tip 2 as compared to tip 1 [Fig. 9(c)]. This directly reflects into a faster thermal ionization for tip 2 as compared to tip 1, the latter presenting a delayed maximum ionization at about 5 ns after laser excitation, consistent with heat diffusion time in silicon [Figs. 8(b) and 8(c)]. Moreover, for tip 2 at $\lambda = 1030$ nm, the absorbed energy density is high both close to the tip apex and about 500 nm far from it [Fig. 9(b)], inducing a first fast rise of its surface temperature, followed by a further slow signal increase [Fig. 9(d)]. This heating is at the origin of an ionization kinetics with a maximum at about 9 ns time delay, again in very good agreement with the experimental one [Fig. 8(d)].

III. CONCLUSION

We have directly measured the optical properties of single nanometric tip-shaped semiconductor samples by spatial modulation spectroscopy. A nonuniform optical extinction along the tip axis, with hot spots in absorption and scattering due to electromagnetic resonances and interference effects, has been experimentally evidenced in agreement with theoretical (analytical and numerical) simulations. A strong change in the absorption properties of silicon tips in the near-IR domain as compared to pure crystalline silicon has also been evidenced, consistent with previous observations on flat silicon surfaces milled by FIB. This optical response is then used to model the heating of the nanometric object after the illumination with a laser pulse, in the framework of La-APT experiments. Complete modeling of a photoexcited carrier and heat diffusion processes allows us to compute the temperature evolution at the tip surface and then quantitatively interpret time-of-flight ionic emission experiments. This explains the delayed and long evaporation reported in La-APT mass spectra, without taking into account more complex processes such as two photon absorption, as previously considered by authors [59].

This study elucidates the contribution of the thermal effects to the complex laser-assisted field evaporation, however, the fast evaporation process corresponding to the first narrow peak still remains unpredicted by our diffusion model. A possible change of the material optical properties under high electric field, influencing the evaporation processes, was reported by Silaeva *et al.* [11]. In the future, SMS analysis on nanometric samples under high electric field (similar to La-APT analysis conditions) could be very useful in identifying such changes in the local optical properties.

Correlation of SMS and La-APT techniques applied to the same type of nano-object gives access to information on both the optical and thermal response of silicon nanotips to the laser illumination. These experiments also show that La-APT can be exploited as a powerful technique to yield the tip temperature evolution at the surface, looking at the dynamics of field ion emission. Combined with SMS experiments, this opens up promising perspectives for the study of the optothermal response of a wide class of individual metallic, semiconducting, or dielectric elongated nano-objects.

[1] B. Desiatov, I. Goykhman, and U. Levy, Nano Lett. **14**, 648 (2014).

[2] R. B. Sadeghian and M. S. Islam, Nat. Mater. **10**, 135 (2011).

[3] H.-C. Han, C.-W. Chong, S.-B. Wang, D. Heh, C.-A. Tseng, Y.-F. Huang, S. Chattopadhyay, K.-H. Chen, C.-F. Lin, J.-H. Lee *et al.*, Nano Lett. **13**, 1422 (2013).

[4] S. Jeong, M. D. McGehee, and Y. Cui, Nat. Commun. **4**, 2950 (2013).

[5] I. Averbukh, B. Chernobrod, O. Sedletsky, and Y. Prior, Opt. Commun. **174**, 33 (2000).

[6] A. V. Zayats, T. Kalkbrenner, V. Sandoghdar, and J. Mlynek, Phys. Rev. B **61**, 4545 (2000).

[7] E. J. Sánchez, L. Novotny, and X. S. Xie, Phys. Rev. Lett. **82**, 4014 (1999).

[8] Y. Yue and X. Wang, Nano Rev. **3**, 11586 (2012).

[9] M. Müller, A. Paarmann, and R. Ernstorfer, Nat. Commun. **5**, 5292 (2014).

[10] D. Ehberger, J. Hammer, M. Eisele, M. Krüger, J. Noe, A. Högele, and P. Hommelhoff, Phys. Rev. Lett. **114**, 227601 (2015).

[11] E. Silaeva, L. Arnoldi, M. Karahka, B. Deconihout, A. Menand, H. Kreuzer, and A. Vella, Nano Lett. **14**, 6066 (2014).

[12] S. Mukherjee, H. Watanabe, D. Isheim, D. N. Seidman, and O. Moutanabbir, Nano Lett. **16**, 1335 (2016).

[13] A. Bouhelier, M. Beversluis, A. Hartschuh, and L. Novotny, Phys. Rev. Lett. **90**, 013903 (2003).

[14] A. Vella, B. Deconihout, L. Marrucci, and E. Santamato, Phys. Rev. Lett. **99**, 046103 (2007).

[15] Y. Kawata, C. Xu, and W. Denk, J. Appl. Phys. **85**, 1294 (1999).

[16] J. Houard, A. Vella, F. Vurpillot, and B. Deconihout, Phys. Rev. B **84**, 033405 (2011).

[17] C. Kealhofer, S. M. Foreman, S. Gerlich, and M. A. Kasevich, Phys. Rev. B **86**, 035405 (2012).

[18] X. Huang, I. El-Sayed, W. Qian, and M. El-Sayed, J. Am. Chem. Soc. **128**, 2115 (2006).

[19] V. A. Ukraintsev and J. T. Yates Jr, J. Appl. Phys. **80**, 2561 (1996).

[20] A. Arbouet, D. Christofilos, N. Del Fatti, F. Vallée, J. R. Huntzinger, L. Arnaud, P. Billaud, and M. Broyer, Phys. Rev. Lett. **93**, 127401 (2004).

[21] J.-C. Blancon, M. Paillet, H. N. Tran, X. T. Than, S. A. Guebrou, A. Ayari, A. San Miguel, N.-M. Phan, A.-A. Zahab, J.-L. Sauvajol, N. Del Fatti, and F. Vallée, Nat. Commun. **4**, 2542 (2013).

[22] Y. R. Davletshin, A. Lombardi, M. F. Cardinal, V. Juvé, A. Crut, P. Maioli, L. M. Liz-Marzán, F. Vallée, N. Del Fatti, and J. C. Kumaradas, ACS Nano **6**, 8183 (2012).

[23] A. Lombardi, M. Loumaigne, A. Crut, P. Maioli, N. Del Fatti, F. Vallée, M. Spuch-Calvar, J. Burgin, J. Majimel, and M. Tréguer-Delapierre, Langmuir **28**, 9027 (2012).

[24] A. Lombardi, M. P. Grzelczak, E. Pertreux, A. Crut, P. Maioli, I. Pastoriza-Santos, L. M. Liz-Marzán, F. Vallée, and N. Del Fatti, Nano Lett. **16**, 6311 (2016).

[25] A. Crut, P. Maioli, N. Del Fatti, and F. Vallée, Chem. Soc. Rev. **43**, 3921 (2014).

[26] A. Lombardi, M. P. Grzelczak, A. Crut, P. Maioli, I. Pastoriza-Santos, L. M. Liz-Marzán, N. Del Fatti, and F. Vallée, ACS Nano **7**, 2522 (2013).

[27] A. Le Beulze, S. Gomez-Graña, H. Gehan, S. Mornet, S. Ravaine, M. Correa-Duarte, L. Guerrini, R. A. Alvarez-Puebla, E. Duguet, E. Pertreux et al., Nanoscale **9**, 5725 (2017).

[28] A. Crut, P. Maioli, F. Vallée, and N. Del Fatti, J. Phys.: Condens. Matter **29**, 123002 (2017).

[29] D. Christofilos, J.-C. Blancon, J. Arvanitidis, A. S. Miguel, A. Ayari, N. Del Fatti, and F. Vallée, J. Phys. Chem. Lett. **3**, 1176 (2012).

[30] J. Giblin, F. Vietmeyer, M. P. McDonald, and M. Kuno, Nano Lett. **11**, 3307 (2011).

[31] T. F. Kelly and D. J. Larson, Annu. Rev. Mater. Res. **42**, 1 (2012).

[32] P. V. Liddicoat, X.-Z. Liao, Y. Zhao, Y. Zhu, M. Y. Murashkin, E. J. Lavernia, R. Z. Valiev, and S. P. Ringer, Nat. Commun. **1**, 63 (2010).

[33] K. Biswas, J. He, I. D. Blum, C.-I. Wu, T. P. Hogan, D. N. Seidman, V. P. Dravid, and M. G. Kanatzidis, Nature (London) **489**, 414 (2012).

[34] Y. Chen, T. Ohkubo, M. Kodzuka, K. Morita, and K. Hono, Scr. Mater. **61**, 693 (2009).

[35] L. M. Gordon and D. Joester, Nature (London) **469**, 194 (2011).

[36] L. Rigutti, I. Blum, D. Shinde, D. Hernández-Maldonado, W. Lefebvre, J. Houard, F. Vurpillot, A. Vella, M. Tchernycheva, C. Durand et al., Nano Lett. **14**, 107 (2013).

[37] E. P. Silaeva, A. Vella, N. Sevelin-Radiguet, G. Martel, B. Deconihout, and T. E. Itina, New J. Phys. **14**, 113026 (2012).

[38] I. Blum, F. Cuvilly, and W. Lefebvre-Ulrikson, in *Atom Probe Tomography*, edited by W. Lefebvre-Ulrikson, F. Vurpillot, and X. Sauvage (Academic, New York, 2016), pp. 97–121.

[39] D. E. Aspnes and A. A. Studna, Phys. Rev. B **27**, 985 (1983).

[40] M. A. Green and M. J. Keevers, Progr. Photovoltaics: Res. Appl. **3**, 189 (1995).

[41] M. A. Green, Sol. Energy Mater. Sol. Cells **92**, 1305 (2008).

[42] D. Pierce and W. E. Spicer, Phys. Rev. B **5**, 3017 (1972).

[43] E. Palik and G. Ghosh, *Handbook of Optical Constants of Solids* (Academic, New York, 1985).

[44] J. Bogdanowicz, M. Gilbert, N. Innocenti, S. Koelling, B. Vanderheyden, and W. Vandervorst, Opt. Express **21**, 3891 (2013).

[45] C. F. Bohren and D. R. Huffman, *Absorption and Scattering of Light by Small Particles* (John Wiley & Sons, New York, 2008).

[46] M. I. Mishchenko, L. D. Travis, and A. A. Lacis, *Multiple Scattering of Light by Particles: Radiative Transfer and Coherent Backscattering* (Cambridge University Press, Cambridge, 2006).

[47] J. Barton, D. Alexander, and S. Schaub, J. Appl. Phys. **66**, 4594 (1989).

[48] R. A. Soref and J. P. Lorenzo, IEEE J. Quantum Electron. **22**, 873 (1986).

[49] J. Schrauwen, D. Van Thourhout, and R. Baets, J. Appl. Phys. **102**, 103104 (2007).

[50] Y. Xiao, F. Fang, Z. Xu, and X. Hu, Appl. Surf. Sci. **343**, 56 (2015).

[51] M. Tamura, S. Shukuri, M. Moniwa, and M. Default, Appl. Phys. A **39**, 183 (1986).

[52] J. I. Pankove, *Optical Processes in Semiconductors* (Courier Corporation, North Chelmsford, MA, 2012).

[53] E. P. Silaeva, N. S. Shcheblanov, T. E. Itina, A. Vella, J. Houard, N. Sevelin-Radiguet, F. Vurpillot, and B. Deconihout, Appl. Phys. A **110**, 703 (2013).

[54] W. Hell, R. Helbig, and M. Schulz, IEEE Trans. Electron Devices **27**, 10 (1980).

[55] B. Gault, F. Vurpillot, A. Vella, A. Bostel, A. Menand, and B. Deconihout, Rev. Sci. Instrum. **77**, 043705 (2006).

[56] E. P. Silaeva, J. Houard, A. Hideur, G. Martel, and A. Vella, Phys. Rev. B **92**, 195307 (2015).

[57] E. P. Silaeva, K. Uchida, Y. Suzuki, and K. Watanabe, Phys. Rev. B **92**, 155401 (2015).

[58] M. K. Miller, A. Cerezo, M. G. Hetherington, and G. D. W. Smith, *Atom Probe Field Ion Microscopy* (Oxford University Press, Oxford, 1996).

[59] T. F. Kelly, A. Vella, J. H. Bunton, J. Houard, E. P. Silaeva, J. Bogdanowicz, and W. Vandervorst, Curr. Opin. Solid State Mater. Sci. **18**, 81 (2014).

[60] M. Kazan, G. Guisbiers, S. Pereira, M. R. Correia, P. Masri, A. Bruyant, S. Volz, and P. Royer, J. Appl. Phys. **107**, 083503 (2010).

[61] H. M. van Driel, Phys. Rev. B **35**, 8166 (1987).

[62] P. Flubacher, A. J. Leadbetter, and J. A. Morrison, Philos. Mag. **4**, 273 (1959).

[63] D. Kingham, Surf. Sci. **116**, 273 (1982).